Ocean Engineering 280 (2023) 114094

Contents lists available at ScienceDirect

Ocean Engineering

journal homepage: www.elsevier.com/locate/oceaneng

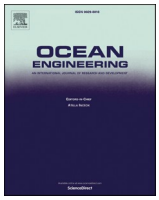

A comparative field study of free-fall cone and sphere penetrometers in soft sediment

S.H. Chow [a,*], C.D. O'Loughlin [b], C.L.V. Goh [c], R. McIlduff [d], D.J. White [e], F.C. Chow [f]

[a] Department of Infrastructure Engineering, Faculty of Engineering and Information Technology, The University of Melbourne, Victoria, 3010, Australia
[b] Industrial Transformational Research Hub for Transforming Energy Infrastructure Through Digital Engineering, Centre for Offshore Foundation Systems, Oceans Graduate School, The University of Western Australia, Crawley, WA, 6009, Australia
[c] Tong Bee Construction Pte Ltd, 37 Tannery Lane #07-01, 347790, Singapore
[d] Arcadis NV Level 5, 225 St Georges Terrace, Perth, WA, 6000, Australia
[e] School of Engineering, University of Southampton, Southampton, SO17 1BJ, UK
[f] Woodside Energy Ltd., Perth, WA, 6000, Australia

ARTICLE INFO

Keywords:
Free-fall penetrometer
Clay
Field tests
Undrained shear strength
Dynamic embedment

ABSTRACT

This paper describes the field performance of two instrumented free-fall penetrometers (FFPs), which offer the possibility of low cost rapid strength profiling without requiring the equipment associated with conventional CPTs or drilling and sampling. The devices considered are a free-fall cone penetrometer (FFcP) and an instrumented free-fall sphere (IFFS). The performance of the FFPs in assessing soil undrained shear strength was investigated and compared through field trials in the soft sediments of the Swan River, Perth, Western Australia. The penetrometers achieved impact velocities of 1.4–5.8 m/s from drop heights of 0.7–3.0 m above the riverbed, and embedded to depths of up to 1.6 times the FFP length (1.45 m) and 4.5 times the IFFS diameter (0.89 m). The FFP data provided the shear strength indirectly using the acceleration measured from an onboard inertial measurement unit. The accuracy depends on the assumptions made regarding the magnitude of dynamic bearing and shaft frictional resistance. Uncertainty associated with dynamic bearing resistance causes a ±10% and ±13% variation in the calculated strength for the IFFS and the FFcP, respectively. However, the equivalent uncertainty in dynamic shaft resistance can cause a variation in the calculated strength of up to ±76% for the FFcP. The FFcP has higher embedment potential than the IFFS, but the IFFS has the advantage of a simpler interpretation without needing to account for dynamic shaft resistance.

1. Introduction

Offshore geotechnical surveys, particularly involving in-situ penetrometer testing, are costly due to the requirement of large specialised vessels that can deploy heavy seabed reaction frames. These costs can be reduced by using free-fall penetrometers (FFPs) that can be deployed more simply, by allowing them to free-fall into the seabed. By including easily deployed FFPs, a site investigation can require fewer conventional push-in penetrometer tests. Also, an FFP campaign can be integrated into other surveys using smaller vessels earlier in a project, obtaining in-situ test data earlier and reducing the requirement to carry design uncertainty.

The last decade has seen a resurgence in FFPs, with numerous systems developed and trialled in the field (e.g. as summarised in Randolph et al., 2018), and an increase in their use on commercial projects (e.g. Young et al., 2011; Jeanjean et al., 2012; Peuchen et al., 2017). These FFPs vary in size and level of instrumentation, ranging from lightweight portable penetrometers deployable by hand but that typically penetrate only by 1–2 m (e.g. Stark et al., 2009; Morton et al., 2016a), to relatively large penetrometers requiring large vessels for deployment, but which provide data to a penetration depth that is comparable to push-in tests (e.g. Stephan et al., 2012; Young et al., 2011). Most FFPs are geometrically slender with conical tips, and resemble their push-in counterpart, a cone penetrometer. Some of these slender penetrometers are 'streamlined' with a reduced shaft diameter further from the tip in an attempt to reduce shaft friction during penetration (e.g. Stephan et al., 2012; Albatal et al., 2020). Alternatively a FFP can be spherical, such as the instrumented free fall sphere (IFFS) (Morton et al., 2016a). The IFFS

* Corresponding author.
E-mail addresses: shiaohuey.chow@unimelb.edu.au (S.H. Chow), conleth.oloughlin@uwa.edu.au (C.D. O'Loughlin), mvincentgohcl@gmail.com (C.L.V. Goh), rian.mcilduff@live.com (R. McIlduff), david.white@soton.ac.uk (D.J. White), fiona.chow@woodside.com.au (F.C. Chow).

https://doi.org/10.1016/j.oceaneng.2023.114094
Received 17 June 2022; Received in revised form 3 February 2023; Accepted 2 March 2023
Available online 14 May 2023
0029-8018/© 2023 The Authors. Published by Elsevier Ltd. This is an open access article under the CC BY-NC-ND license (http://creativecommons.org/licenses/by-nc-nd/4.0/).

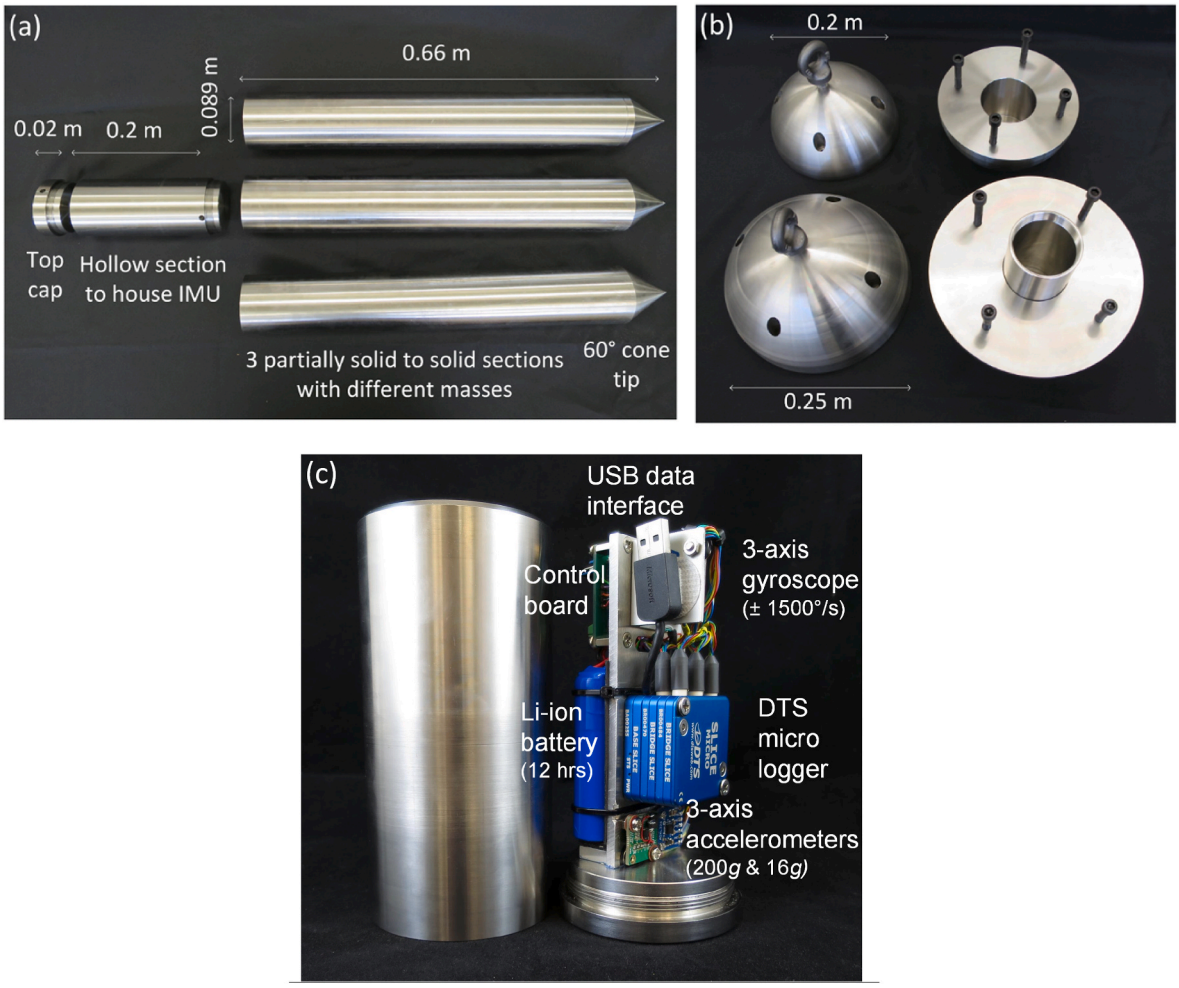

Fig. 1. (a) Free-fall cone penetrometer (FFcP); (b) instrumented free-fall sphere (IFFS); and (c) Inertial measurement unit (IMU).

is somewhat similar to a push-in ball penetrometer, but with the penetrometer rods replaced by a tether. In this way, the IFFS exploits some of the advantages of full-flow ball penetrometers over cone penetrometers (Randolph et al., 2011), but also the data quality is less vulnerable to rotation of the device as the projected area remains the same regardless of the sphere orientation.

FFP test interpretation methods have been developed and improved through experimental studies in the laboratory (e.g. Dayal and Allen, 1973; Chow and Airey, 2014; Chow et al., 2014; Chow et al., 2017; Morton et al., 2016b; Albatal et al., 2020) and in the field (e.g. Stephan et al., 2012; Stark et al., 2009; Morton et al., 2016a). These studies demonstrate that the accuracy and complexity of the data interpretation is dependent on both the penetrometer geometry and the level of instrumentation. Most FFPs are only instrumented with accelerometers, so the soil strength is derived indirectly from acceleration measurements by solving the equations of motion. For FFPs with more sophisticated instrumentation (e.g. Stegmann et al., 2006; Chow et al., 2017; Peuchen et al., 2017), the soil strength can be determined directly from tip load cell measurements.

This study compares the performance of conical and spherical FFPs through field deployments in a riverbed in Perth, Western Australia. The accuracy of the interpreted riverbed strength profiles is assessed by comparison with data from push-in piezocone tests.

2. Development of free-fall penetrometers

The two FFPs were fabricated from stainless steel and are relatively light (<60 kg), to enable deployment from smaller vessels using non-specialist equipment. The first penetrometer is a free-fall cone penetrometer (FFcP) with a cone and shaft diameter, $d = 0.089$ m and a total length, $L = 0.88$ m such that the aspect ratio, $L/d \sim 10$ (Fig. 1a). The diameter was selected to accommodate the instrumentation package (an inertial measurement unit, IMU) described later. The FFcP is comprised of three sections; a lower 0.66 m long section with a 60° conical tip, a 0.2 m long middle section to accommodate the IMU, and an upper top cap, 0.02 m long, that provides access to the IMU and accommodates the tether connection. The design is modular, with three separate lower sections that vary in mass (with different internal voids) such that the total mass is $m = 24.5$, 30.7 or 36.6 kg. O-rings are used in the threaded connections between each section to prevent water ingress.

The second penetrometer is an instrumented free-fall sphere (IFFS), based on the design described in Morton et al. (2016a), and available with a diameter, $D = 0.2$ or 0.25 m, with a corresponding mass, $m = 29.4$ or 56 kg. The sphere consists of two hemispheres bolted together with an internal vertically oriented cylindrical void to accommodate the IMU (see Fig. 1b). As with the FFcP, an O-ring located between the two hemispheres prevents water ingress.

2.1. Instrumentation

The IMU is a self-contained motion logger designed for free-fall projectiles (Fig. 1c). The IMU measures acceleration along three orthogonal axes, and rotation rates about the same three axes using a combination of micro-electromechanical system (MEMS) rate

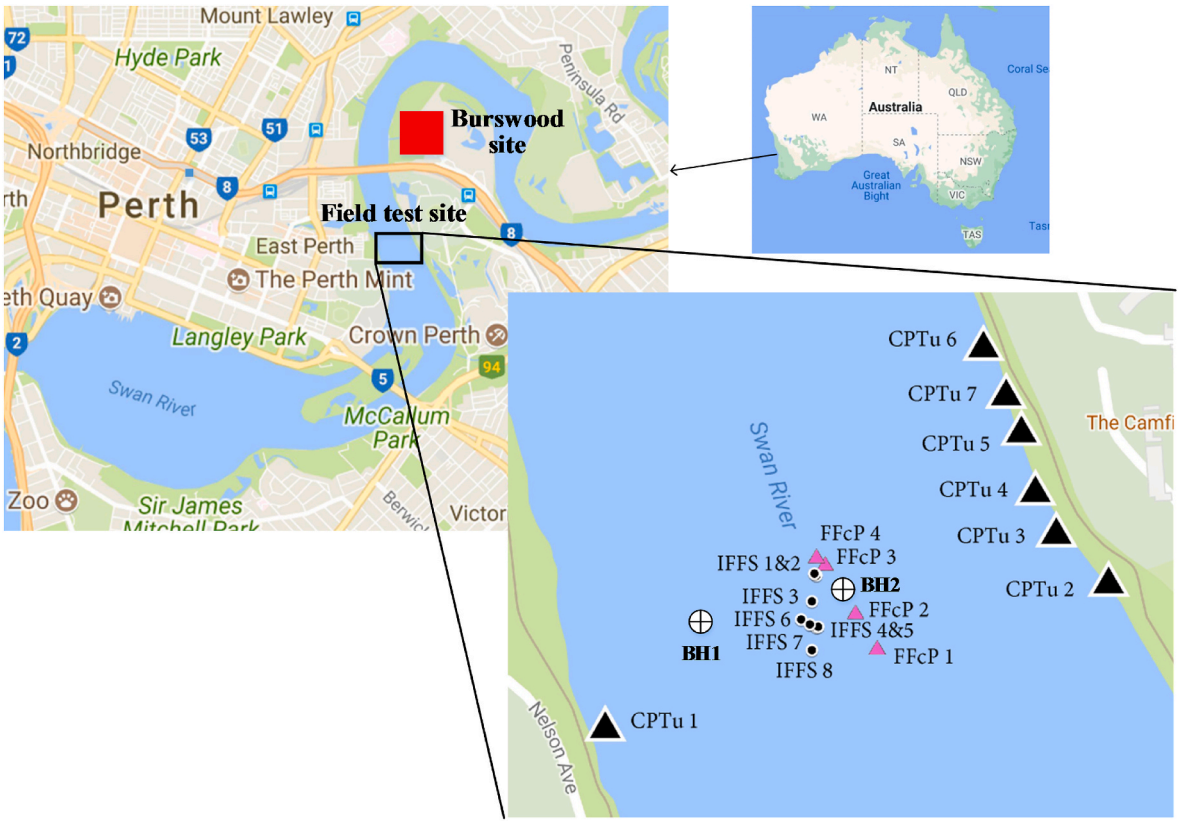

Fig. 2. Test site showing locations of existing boreholes (BH), piezocone penetrometer tests (CPTu), and free-fall penetrometer tests (FFcP and IFFS).

gyroscopes and accelerometers. These measurements, after processing, provide the projectile trajectory during free-fall in water and embedment into the sediment (Blake et al., 2016), as well as an indirect estimation of the undrained shear strength profile (e.g. Morton et al., 2016a). The device is equipped with two 13-bit three-axis MEMS accelerometers. The first accelerometer (ADXL326) has a resolution of 0.004*g* with a measurement range of ±16*g* and the second accelerometer (ADXL377) has a resolution of 0.05*g* with a measurement range of

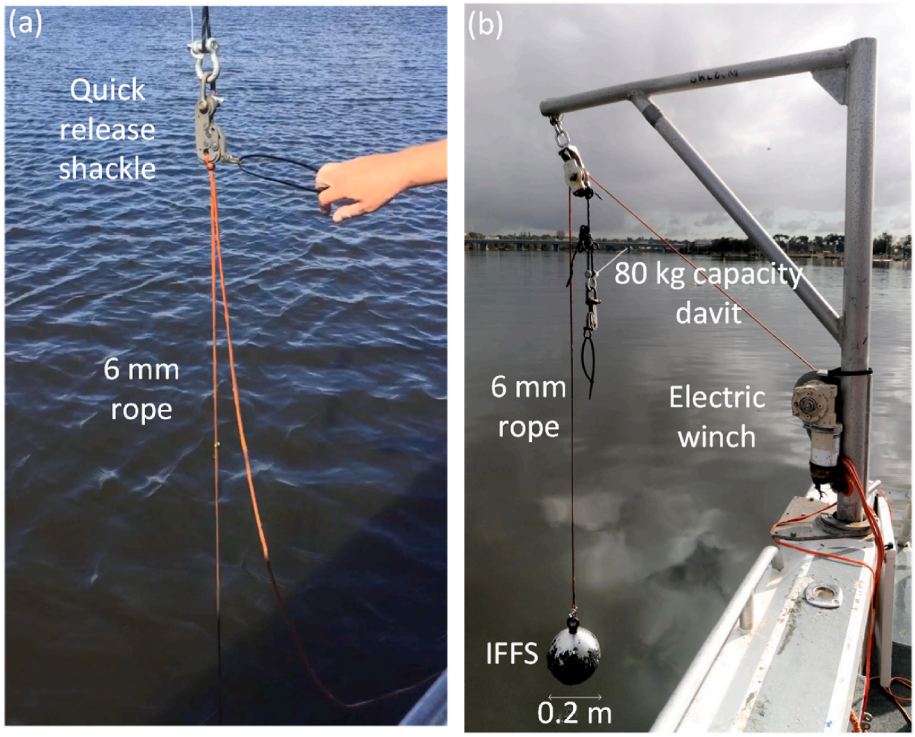

Fig. 3. Field testing arrangement: (a) deployment via quick release shackle; (b) retrieval.

Table 1
Field test program and results.

Penetrometer/test ID	Mass, m (kg)	Water depth, s_w (m)	Fall height, s_f (m)	Impact velocity, v_i (m/s)	Final embedment depth, z_e (m)	Embedment ratio, z_e/L or z_e/D[a]
FFcP 1	30.70	3.3	1.34	4.31	0.191	0.22
FFcP 2	30.70	3.1	2.46	5.32	0.252	0.29
FFcP 3	30.70	3.2	2.93	5.72	1.306	1.48
FFcP 4	30.70	3.2	1.60	4.85	1.451	1.65
IFFS 1	29.42	3.3	0.72	1.43	0.423	2.12
IFFS 2	29.42	3.2	2.63	5.32	0.892	4.46
IFFS 3	29.42	3.3	2.60	5.42	0.820	4.10
IFFS 4	29.42	3.6	1.92	5.03	0.675	3.38
IFFS 5	29.42	3.6	0.90	3.59	0.398	1.99
IFFS 6	29.42	3.5	2.86	5.77	0.624	3.12
IFFS 7	29.42	3.5	0.89	2.06	0.313	1.57
IFFS 8	29.42	3.4	1.82	4.72	0.303	1.52

[a] $L = 0.88$ m for the FFcP, $D = 0.2$ m for the IFFS.

$\pm 200g$, such that the IMU can appropriately cater for sediments of different strengths. The $\pm 16g$ accelerometer was used in this study as soft sediment was expected at the test locations. Two 16-bit dual-axis MEMS rate gyroscopes (LPR5150AL) with a resolution of 0.05°/s and a measurement range of ±1500°/s allow roll, pitch and yaw rotations to be determined. The accelerometer and gyroscope data were logged at 1 kHz using a Diversified Technical Systems (DTS) data acquisition system (DAS). This logging frequency allows for 300 h of data collection before the 16 Gb of onboard memory is exhausted, but is limited to ~12 h due to the capacity of the lithium-ion battery that powers the DAS. The DTS DAS is very compact, measuring only 42 × 42 × 22 mm for six channels of data measurement. The complete IMU fits within a watertight stainless steel tube, 170 mm long and 78 mm in diameter.

3. Field test details

3.1. Test location

The free-fall penetrometer tests were conducted in the Swan River in Perth, Western Australia. The locations for all FFcP tests, IFFS tests and pre-existing boreholes are shown in Fig. 2, where the water depths varied between 3.1 and 3.6 m. Fig. 2 also shows the locations where push-in piezocone tests, were conducted previously along the shoreline up to 200 m away from the FFP tests. Boreholes at close vicinity to the test sites indicates that the upper 2.5 m of the riverbed at this location is a silty sandy CLAY (with 50% shell fragments) of high plasticity (BH1), or a clayey SILT (with traces of fine grained sand and shell fragments) of high plasticity (BH2). Other available index properties for the sediment include: a natural moisture content of approximately 87%, specific gravity of 2.58 and unit weight of approximately 14.6 kN/m^3. The sediment properties are very similar to Burswood clay (Low et al., 2011), which is located within 1 km from the test site as indicated in Fig. 2.

3.2. Test procedure

The FFP tests were conducted from the RV BF Ryan, an 8 m research vessel equipped with a 80 kg capacity davit fitted with an electronic winch system. A 6 mm diameter Dyneema synthetic rope was used as the FFP deployment and retrieval line. Deployment was achieved by pulling on a quick-release shackle connected to the loading hook of the davit arm (Fig. 3). The test setup is shown in Fig. 3 and the test procedure is summarised below:

1. The IMU was powered and secured in the penetrometer;

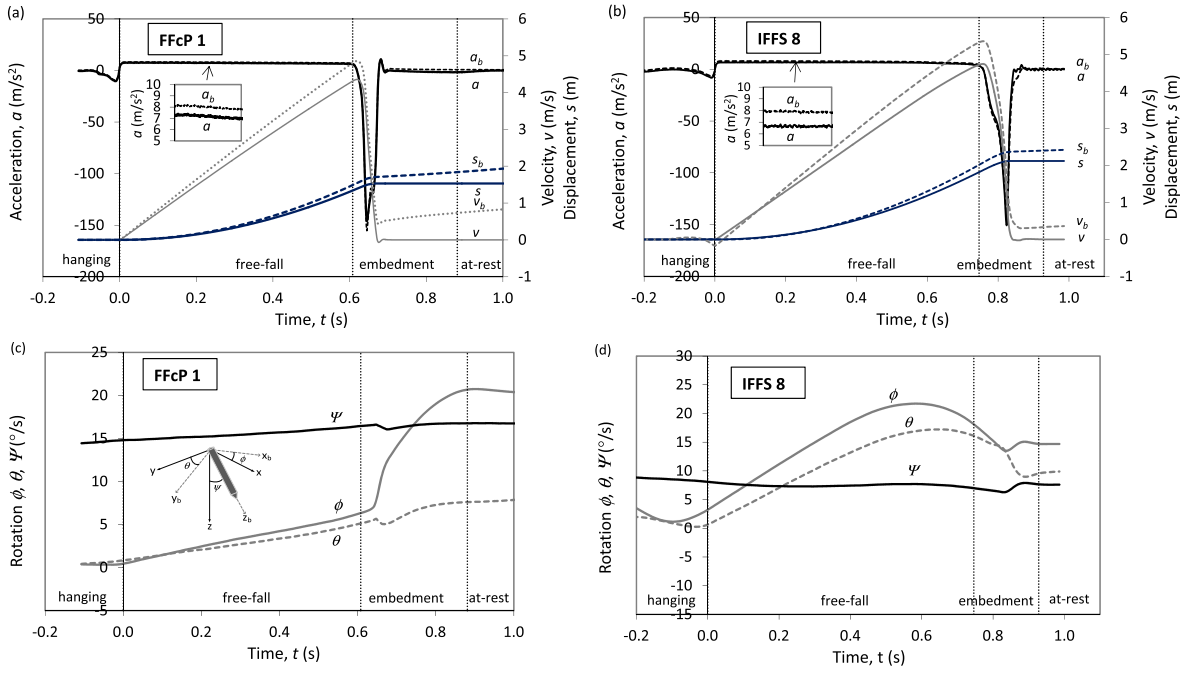

Fig. 4. Typical motion and rotation profiles for: (a) (c) test FFcP 1; and (b) (d) test IFFS 8.

2. The penetrometer was attached to the quick release system and lowered in the water to the pre-determined drop height;
3. After ensuring there was sufficient slack in the deployment line, the quick release shackle was opened (Fig. 3a), allowing the penetrometer to free-fall and embed into the sediment;
4. Penetrometer embedment depth was estimated by pulling the rope taut and noting identifier markings on the rope at the waterline;
5. The penetrometer was retrieved using the electric winch (Fig. 3b);
6. The vessel was then moved to the next test location and steps 2–5 repeated;
7. At the end of testing or upon switching penetrometer, the IMU was retrieved and the data downloaded.

A typical FFP test employing the above procedure (steps 2–5) takes about 10–15 min, depending on weather conditions.

3.3. Test program

The field test program is summarised in Table 1 and includes four FFcP and eight IFFS tests with fall heights varied to achieve impact velocities, v_i ~1.4–5.8 m/s. To enable direct comparison between the two penetrometers, the field tests involved penetrometers with comparable masses, the FFcP with $m = 30.7$ kg and the 0.2 m diameter IFFS with $m = 29.4$ kg.

4. Field measurements

The field test results are summarised in Table 1 in terms of the penetrometer mass, m, the water depth, s_w (measured using the vessel's onboard acoustic echo sounder which has a resolution of approximately 0.1 m), fall height, s_f, impact velocity, v_i, final embedment depth, z_e interpreted from the IMU data, and embedment ratio, z_e/L (FFcP) or z_e/D (IFFS). The IMU data were interpreted using the framework described in Blake et al. (2016), which allows the 3-dimensional motion (x, y, z) of the FFPs to be transformed from a non-stationary body reference frame of the IMU (and consequently of the penetrometer) to a fixed inertial reference frame defined with the z-axis aligned in the direction of the Earth's gravitational vector. This transformation from a moving body frame of reference to a fixed inertial frame of reference is needed to avoid erroneous determinations of distance travelled, and also erroneous determinations of undrained shear strength from accelerometer data (Blake et al., 2016).

MEMS accelerometers measure both constant acceleration (e.g. Earth's gravity) and changing acceleration (due to motion). Hence, the acceleration needed in the interpretation of FPP data is the acceleration due to motion, which requires that $g = 9.81$ m/s^2 is subtracted from the acceleration in the z axis of the inertial frame of reference. Here we use the term 'acceleration' and the notation, a, to describe acceleration due to motion. Penetrometer velocity, v, and displacement, s, can then be determined in either the body or inertial frame of reference by numerically integrating the acceleration (once for velocity and twice for displacement).

Typical time histories of acceleration, a, velocity, v and displacement, s for the FFcP and IFFS are shown in Fig. 4a and b in the z-axis of both the body (with subscript b) and inertial frames of reference. Acceleration, a, becomes non-zero at the point of release ($t \approx 0$ s), partly due to the motion from opening the quick-release shackle, but then approaches a ~7.6 m/s^2 during free-fall in water, noting that $a < g$ during free-fall in water due to the fluid drag resistance acting on the penetrometer and on the trailing rope.

The acceleration immediately reduces upon impacting the riverbed, reaching a maximum deceleration, $a = -146$ m/s^2 (FFcP 1) and $a = -151$ m/s^2 (IFFS 8) before coming to rest. The velocity, v and displacement, s, are noticeably different in the body and inertial reference frames during free-fall in water and when the penetrometers come to rest, indicating that the penetrometers were non-vertical during free-fall.

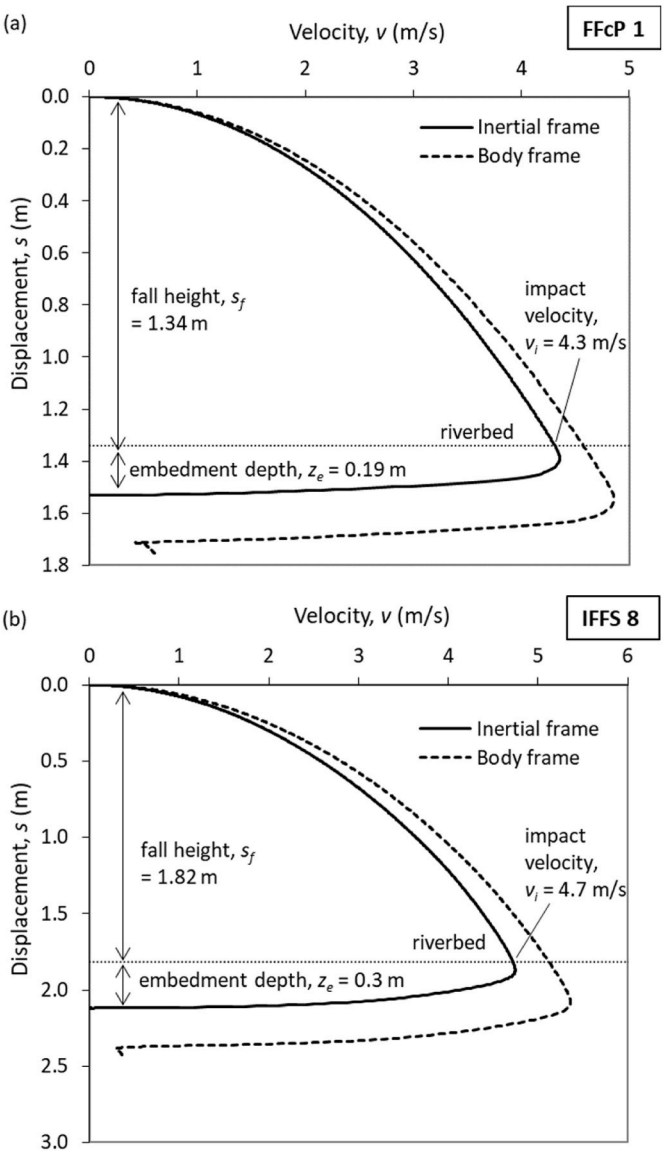

Fig. 5. Typical velocity-displacement profiles: (a) test FFcP 1; (b) test IFFS 8.

To further explore the verticality of the penetrometers during the tests, the corresponding time histories of rotation for tests FFcP 1 and IFFS 8 are presented in Fig. 4c and d, with ϕ, θ, and ψ representing the pitch, roll, and yaw rotations about the inertial frame axes x, y, and z as defined in Blake et al. (2016). The x and y axes lie in the horizontal plane, and the z axis is initially vertical.

Prior to release, the FFcP and IFFS were swaying in water, registering angles of ψ ~15° and ~9° from the vertical respectively. Despite concerns that operating the quick-release shackle would lead to a side-pull on the deployment line that would cause additional rotation, the maximum change in rotation for the FFcP was about 6° during free-fall in water. Although the IFFS experienced greater rotations of up to around 22° during free-fall, the spherical geometry ensures that there is no change in the projected area.

During penetration in soil, the FFcP continued to rotate (changing ϕ and θ), but only deviated slightly more from the vertical, such that the maximum rotation was $\psi \sim 17°$ when at rest in the soil. Impact with the riverbed led to a rotation 'correction' for the IFFS, although as noted previously, rotation of the sphere will not affect analysis of the IFFS measurements provided the interpretation considers a fixed inertial

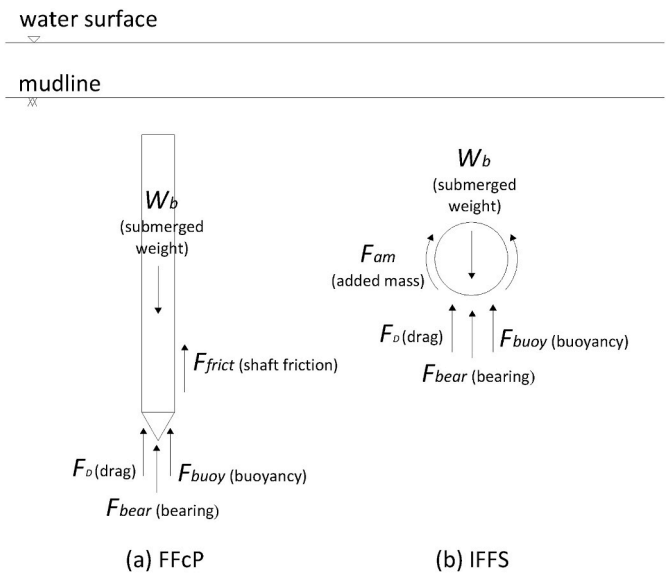

Fig. 6. Forces acting on the free-fall penetrometers during embedment in soil: (a) FFcP; and (b) IFFS.

reference frame. FFcP rotation can be reduced by adding stabilizing fins to encourage self-straightening during free-fall in water, as confirmed through the minimal rotations measured in a later (unpublished) study where the FFcP included stabilizing fins.

These measured rotations highlight the importance of considering the motions within a fixed or inertial reference frame as shown in Fig. 5, which plots the same data as profiles of velocity, v with displacement, s. Fig. 5 shows that an interpretation within a body frame of reference would lead to a gross overestimation of impact velocity, v_i by up to 13% and of embedment (in sediment), z_e by up to 14%, consistent with Blake et al. (2016).

5. Undrained shear strength determination from free-fall measurements

The profile of undrained shear strength, s_u, with depth can be determined indirectly for both the FFcP and IFFS tests by considering the force balance on the penetrometer:

$$ma = W_b - F_{resist} \tag{1}$$

where m is the penetrometer mass, a is acceleration in the inertial frame of reference, W_b is the penetrometer weight submerged in water and F_{resist} is the sum of the various resisting forces acting on the penetrometer. These forces depend on the penetrometer geometry (Fig. 6).

(a) FFcP

For the FFcP, Eq. (1) may be written as (Chow et al., 2017):

$$ma = W_b - F_{bear} - F_{frict} - F_D - F_{buoy} \tag{2}$$

where the resisting forces are bearing resistance at the cone tip (due to soil strength), F_{bear}, frictional resistance along the shaft, F_{frict}, drag resistance, F_D, and a buoyancy force, F_{buoy}, equal to the effective weight of the soil displaced by the advancing penetrometer. The inclusion of the drag resistance term, F_D, in Eq. (2) is warranted, particularly for very soft sediments, and has been shown to be the dominant resistance acting on a dynamically installed anchor in normally consolidated clay over about one-third of the penetration (Blake and O'Loughlin, 2015).

Bearing and frictional resistances are expressed as:

$$F_{bear} = R_{f(bear)}\left(s_u N_{kt} A_t\right) \tag{3}$$

$$F_{frict} = R_{f(frict)}\left(\alpha s_{u(avg)} A_s\right) \tag{4}$$

where A_t and A_s are the tip and shaft areas respectively, N_{kt} is the cone factor, α is the interface friction ratio, s_u is the undrained shear strength at the cone tip and $s_{u(avg)}$ is the average strength over the length of the embedded shaft. $R_{f(bear)}$ and $R_{f(frict)}$ in Eqs. (3) and (4) are power-law strain rate formulae to account for the well-known dependence of soil strength on strain rate (Biscontin and Pestana, 2001) expressed as:

$$R_{f(bear)} = \left(\frac{(v/d)}{(v/d)_{ref}}\right)^{\beta_{bear}} \geq 1 \tag{5}$$

$$R_{f(frict)} = \left(\frac{(v/d)}{(v/d)_{ref}}\right)^{\beta_{frict}} \geq 1 \tag{6}$$

where the (v/d) terms are proxies for strain rate, d is the penetrometer diameter, and β_{bear} and β_{frict} are strain rate parameters for bearing and frictional resistance respectively. The $(v/d)_{ref}$ term represents the average strain rate in the equivalent test used to measure the (reference) undrained shear strength, typically an in-situ push-in penetrometer test.

The drag resistance term is formulated as

$$F_D = \frac{1}{2}\rho_s C_D A_t v^2 \tag{7}$$

where ρ_s is the saturated density of the soil and C_D is the drag coefficient.

The soil buoyancy force, F_{buoy}, is calculated as the effective weight of the displaced soil:

$$F_{buoy} = \rho' V_s g \tag{8}$$

where ρ' is the submerged density of soil and V_s is the volume of soil displaced by the penetrometer. V_s is equal to the sum of the currently submerged penetrometer volume and of the cavity formed in the wake of the advancing penetrometer. Here we assume that the soil does not flow back behind the penetrometer over the very short installation duration (O'Loughlin et al., 2013), such that V_s is calculated assuming a cylindrical cavity with a height from the trailing edge of the penetrometer to the mudline and with a diameter, d.

(b) IFFS

The forces acting on the IFFS during dynamic embedment in soil are shown in Fig. 6b. The equation of motion for the IFFS in Eq. (9) is an expanded form of the solution formulated in Morton et al. (2016b):

$$ma = W_b - F_{sb} - F_{am} - F_{bear} - F_D \tag{9}$$

where F_{bear} is now the bearing resistance acting on the frontal area of the sphere and the additional term, F_{am}, is an added mass force that accounts for the soil that accelerates or decelerates with the IFFS (noting that it is negligible for the FFcP due to its slender geometry; Blake and O'Loughlin, 2015). F_{am} is calculated as:

$$F_{am} = aC_m m_{soil} \tag{10}$$

where a is the acceleration in the inertial frame of reference as defined previously, C_m is the added mass coefficient and m_{soil} is the product of the soil density and the volume of the sphere. As discussed in Morton et al. (2016b), the F_{bear} and F_D terms can be combined via a superposition approach in which the strength and drag resistance components are simply summed into a single resistance force, F_r:

$$F_r = NA_b R_{f(bear)} s_u \tag{11}$$

where A_b is the frontal or bearing area of the sphere, $R_{f(bear)}$ is the power-law strain rate function for bearing resistance (Eq. (5)), s_u is the undrained shear strength corresponding to the equator depth on the sphere and N is a single capacity factor defined as:

Table 2
Model parameters for undrained shear strength determination.

Model parameter	FFcP	IFFS
N_{kt} (Eq. (3)) or N_c (Eq. (12))	11.2	10.9
α (Eq. (4))	0.22	–
β_{bear} (Eq. (5))	0.06	0.06
β_{frict} (Eq. (6))	0.21	–
C_D (Eq. (7))	1.20	0.26
C_m (Eq. (10))	–	0.5
ρ_s	1487 kg/m^3	1487 kg/m^3

$$N = \frac{1}{2} C_D R_{e(non-Newtonian)} + N_c \tag{12}$$

N_c in Eq. (12) is the conventional bearing capacity factor used to link net penetration resistance to undrained shear strength (analogous to the cone factor, N_{kt} in Eq. (3)) and $R_{e(non\text{-}Newtonian)}$ is the non-Newtonian Reynolds number, defined as $R_{e(non\text{-}Newtonian)} = \rho_s v^2 / s_u R_{f(bear)}$.

5.1. Model parameters

Undrained shear strength, s_u, can be determined using Eq. (2) and Eq. (9) for the FFcP and the IFFS respectively. FFcP interpretation requires the appropriate selection of four additional parameters beyond that required for push-in cone data; α, β_{bear}, β_{fric} and C_D. A complete interpretation also requires selection of an appropriate cone factor, N_{kt}, and a soil density, ρ_s, as required for push-in cone data. Interpretation of IFFS data requires only two extra parameters relative to a push-in ball test; β_{bear} and C_D. As with the FFcP, IFFS interpretation requires a bearing factor, N_c and soil density, ρ_s, as for a push-in ball test (the latter for determination of net penetration resistance).

Both the FFcP and IFFS formulation require the nomination of a (proxy) reference strain rate, $(v/d)_{ref}$. In the context of attempting to obtain the equivalent s_u as from a push-in test, $(v/d)_{ref}$ should use a typical CPT velocity and diameter. Here we assume a 10 cm^2 cone penetrated at the standard 20 mm/s, such that $(v/d)_{ref} = 20/35.7 = 0.56$ s^{-1}. This is two orders of magnitude lower than the maximum strain rate in the free-fall tests, which is an appropriate magnitude of adjustment using the power-law strain rate formula (O'Beirne et al., 2017a).

A laboratory-determined soil strength could be used for the reference value. This would involve a much lower strain rate (typically 10^{-6} s^{-1}), such that Eqs. (5) and (6) would be applied over seven orders of magnitude. Despite the much higher strain rates associated with a push-in penetrometer test, laboratory (element) soil strengths are typically similar in magnitude to push-in penetrometer soil strengths, due to the compensating effect of strain softening. Consequently, applying Eqs. (5) and (6) with a laboratory reference strain rate would over-quantify the strain rate effect and lead to a much lower and erroneous soil strength.

The model parameters are summarised in Table 2. Owing to the close proximity of the site to the well-characterised Burswood soft clay research site, many of the model parameters are selected on the basis of knowledge of this soil (Low et al., 2011). If prior knowledge is not available, the model parameters can be estimated based on established ranges reported for other similar sediments in the literature. Further discussion on the uncertainty of these parameters can be found in Chow et al. (2017). The interface friction ratio for the FFcP is taken as $\alpha = 1/S_t = 0.22$, where $S_t = 4.5$ is the soil sensitivity derived from vane shear tests on Burswood clay (Low et al., 2011). The strain rate parameter for bearing resistance is taken as $\beta_{bear} = 0.06$ for both the FFcP and the IFFS, on the basis of variable rate T-bar and ball penetration field tests conducted in Burswood clay (Low et al., 2008). Centrifuge FFcP tests in kaolin clay reported in Chow et al. (2017) show that the strain rate parameter for shaft resistance is 3.5 times that for tip resistance, i.e. $\beta_{frict}/\beta_{bear} = 3.5$, and this ratio was applied in these field tests, such that $\beta_{frict} = 0.21$. Cone and ball factors were taken as $N_{kt} = 11.2$ and $N_c = 10.9$, consistent with interpretation of field piezocone and piezoball tests

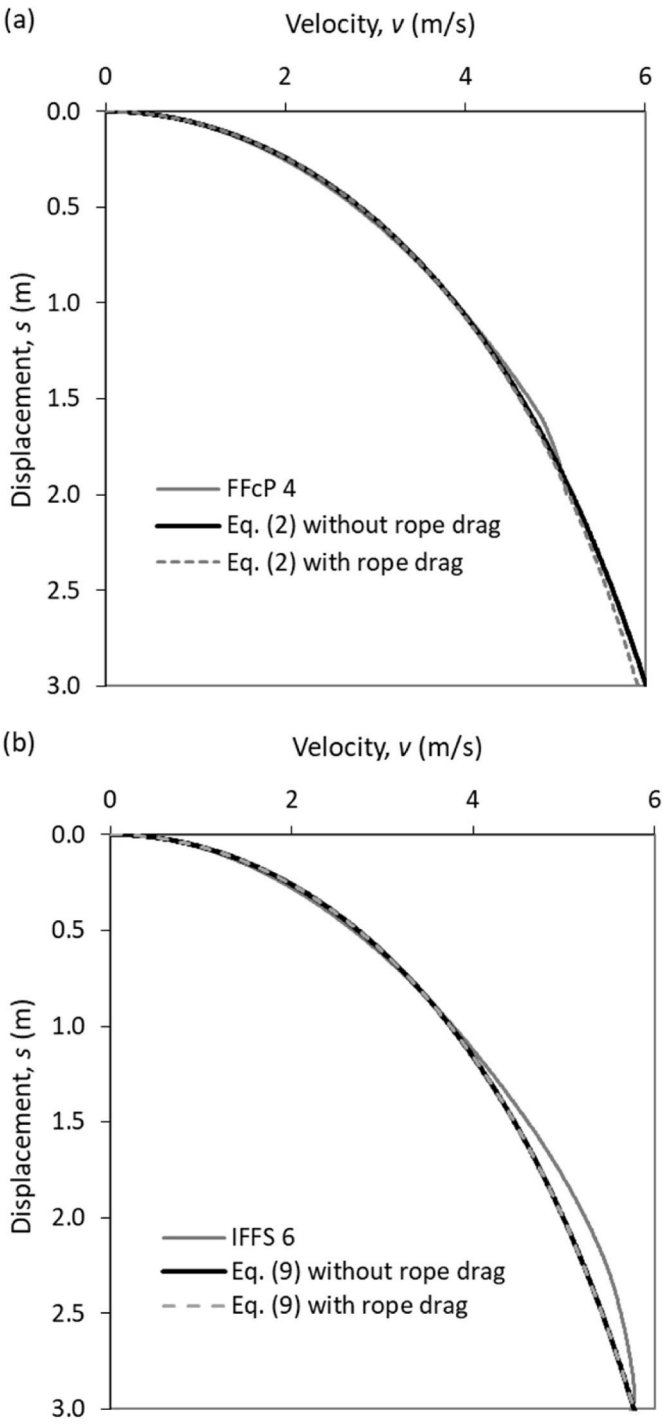

Fig. 7. Measured and calculated (with and without rope drag) velocity profiles during free-fall in water: (a) FFcP; and (b) IFFS.

in Burswood clay (Low et al., 2011). Soil density was established from specific gravity and moisture content measurements made during a previous site investigation. Although adjustment for N_c or N_{kt} during shallow penetration can be made (e.g. Morton et al., 2016a; Guo et al., 2022), a simplified approach assuming depth independent N_c or N_{kt} values was adopted here, such that the resulting calculations of s_u should be considered as conservative.

A drag coefficient, C_D, may be selected from theoretical or numerical solutions. Alternatively, a value may be determined from fits to the measured motion in water using Eq. (2) (FFcP) and Eq. 9 (IFFS), but where the soil resistance terms are omitted and the drag resistance, F_D,

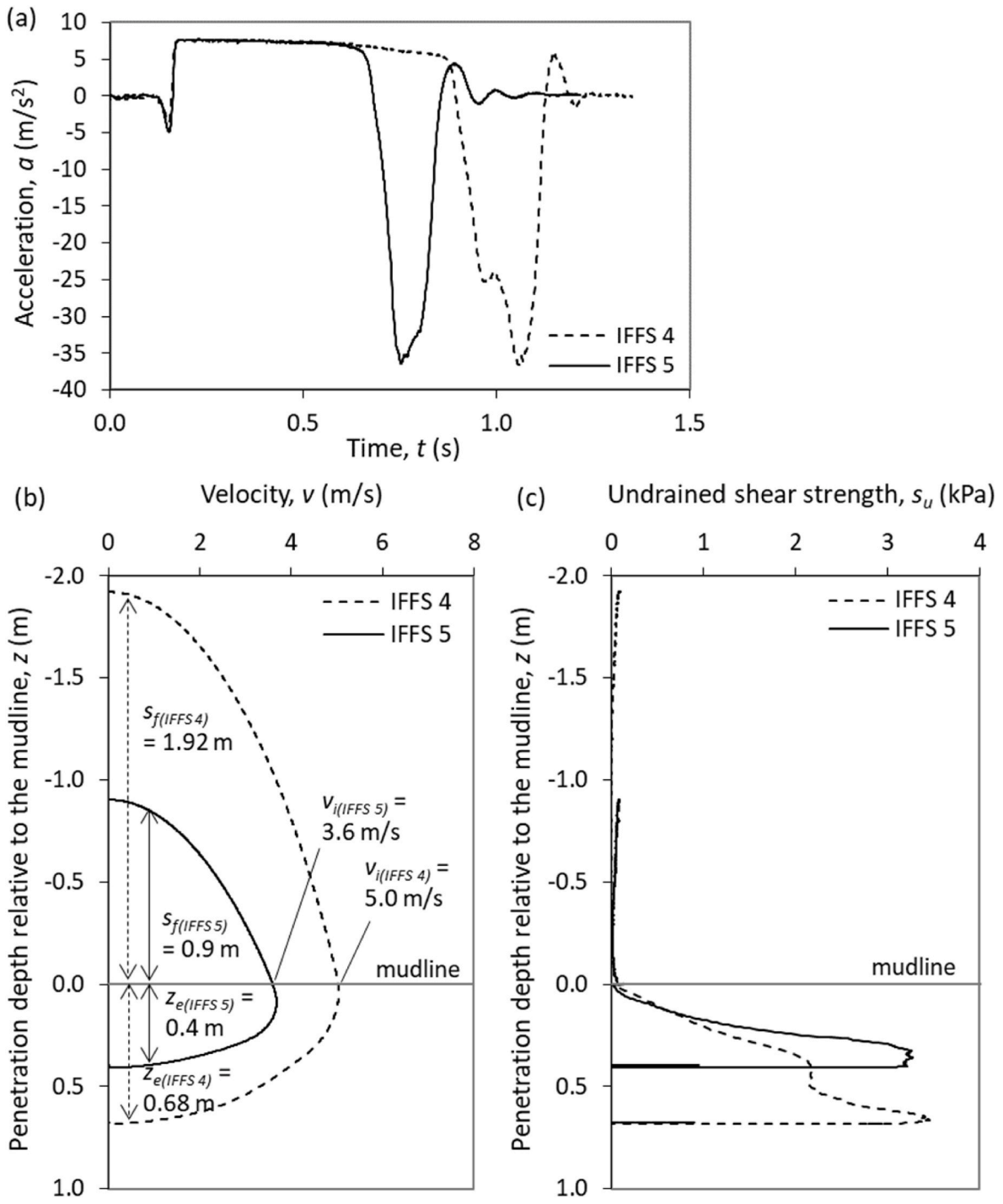

Fig. 8. Effect of impact velocity on embedment for the IFFS: (a) acceleration signatures; (b) velocity profiles; (c) interpreted undrained shear strength profiles.

uses the density of water rather than soil. That approach is adopted here, with good agreement obtained using drag coefficients of $C_D = 1.2$ for the FFcP (Fig. 7a) and $C_D = 0.26$ for the IFFS (Fig. 7b). The added mass term, F_{am} (Eq. (10)), was also considered for the IFFS to account for the mass of soil accelerated with the sphere. Theoretical solutions give $C_m = 0.5$ for a sphere (e.g. Sumer and Fredsoe, 1997), which has been shown to work well for the IFFS (Morton et al., 2016a) during freefall in water using the mass of water, m_{water}, rather than m_{soil} in Eq. (10). Drag resistance on the trailing rope may also be considered, although as shown in O'Beirne et al. (2017b) the effect is only significant when the free-fall in water distance is large relative to the length scale of the penetrometer. This is evident from Fig. 7, where alternative theoretical velocity profiles show that rope drag resistance (using a drag coefficient for the rope, $C_D = 0.019$; O'Beirne et al., 2017b) has negligible effect over the 3 m free-fall distance.

The back-fitted $C_D = 0.26$ for the IFFS is identical to that determined from IFFS field tests reported in Morton et al. (2016a). However, the back-fitted $C_D = 1.2$ for the FFcP is much higher than that expected for a cone tipped slender cylinder; e.g. $C_D = 0.22$ from computational fluid dynamic analyses of a slender cylinder (length/diameter = 12.5) with a conical tip at comparable velocities (Richardson, 2008). The higher C_D in this study is considered to be due to FFcP tilt (Fig. 4c), noting that the average tilt for the four FFcP tests was $\psi = 19.7°$ during free-fall in water. Accounting for this tilt using the effective projected drag area

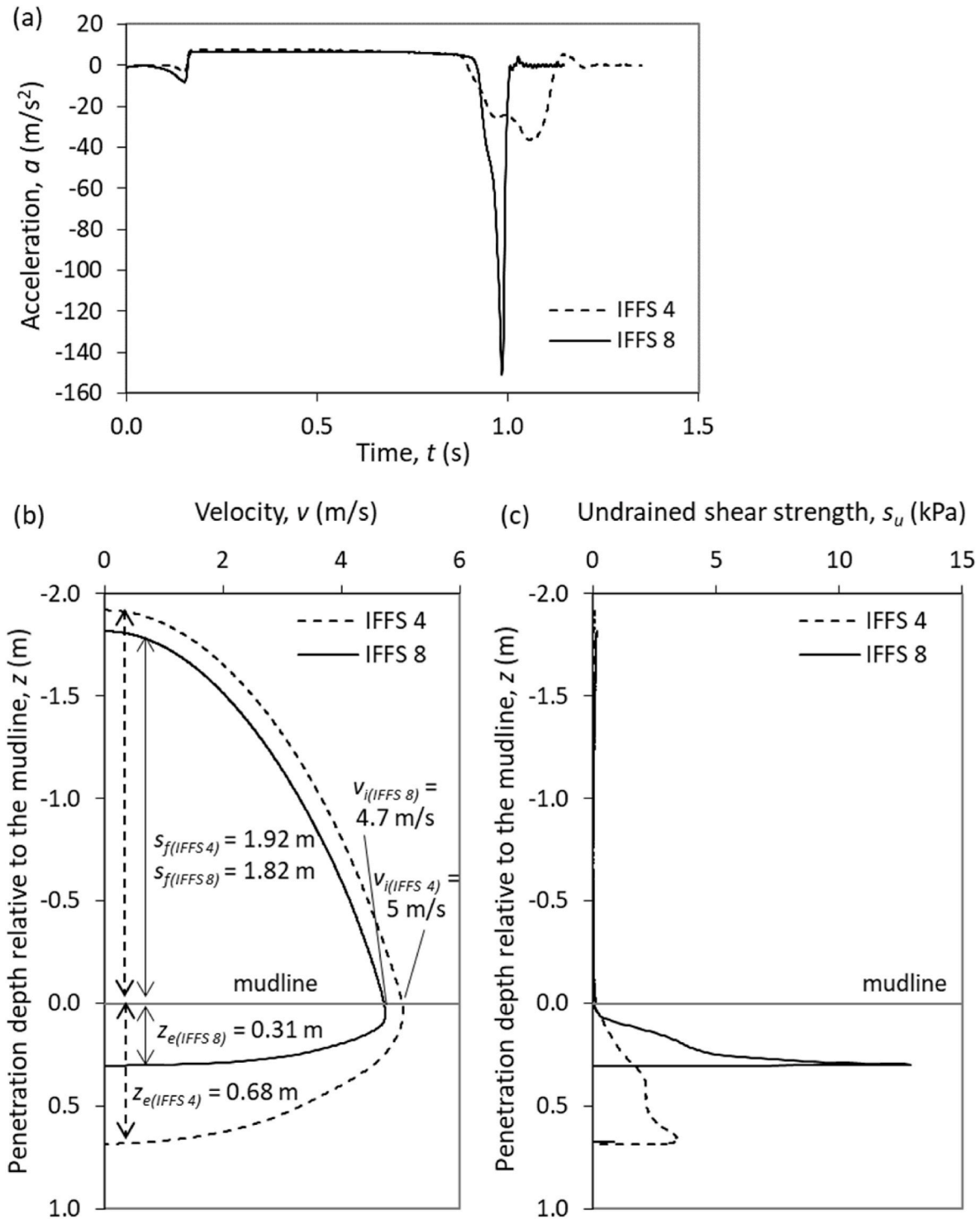

Fig. 9. Effect of sediment strength on: (a) acceleration signatures; (b) velocity profiles; (c) interpreted undrained shear strength profiles.

($Ld\sin\psi$) instead of the FFcP tip area in Eq. (7), results in an equivalent but lower $C_D = 0.28$, in reasonable agreement with $C_D = 0.22$ determined numerically by Richardson (2008).

5.2. Undrained shear strength profiles

Figs. 8c to 10c show s_u profiles derived using the above approaches, from release in water to final embedment in sediment. In water s_u is negligible indicating that the interpretation approach accounts correctly for fluid resistance. A marked increase in s_u is evident upon impact with the sediment, providing reliable mudline detection.

The effect of impact velocity, v_i, or fall height, s_f, on embedment is illustrated in Fig. 8 by tests IFFS 5 and IFFS 4, which were within 1 m proximity, but achieved different impact velocities, $v_i = 3.6$ and 5 m/s, from different fall heights, $s_f = 0.9$ m and 1.92 m. The similar peak deceleration between the two tests suggests the sediment is similar (as discussed later), albeit that the sediment appears to become stronger at a greater depth at the IFFS4 test location. The increase in final embedment depth, z_e, from 0.4 to 0.68 m shows the benefit of a greater fall height when operating below the terminal velocity of the penetrometer,

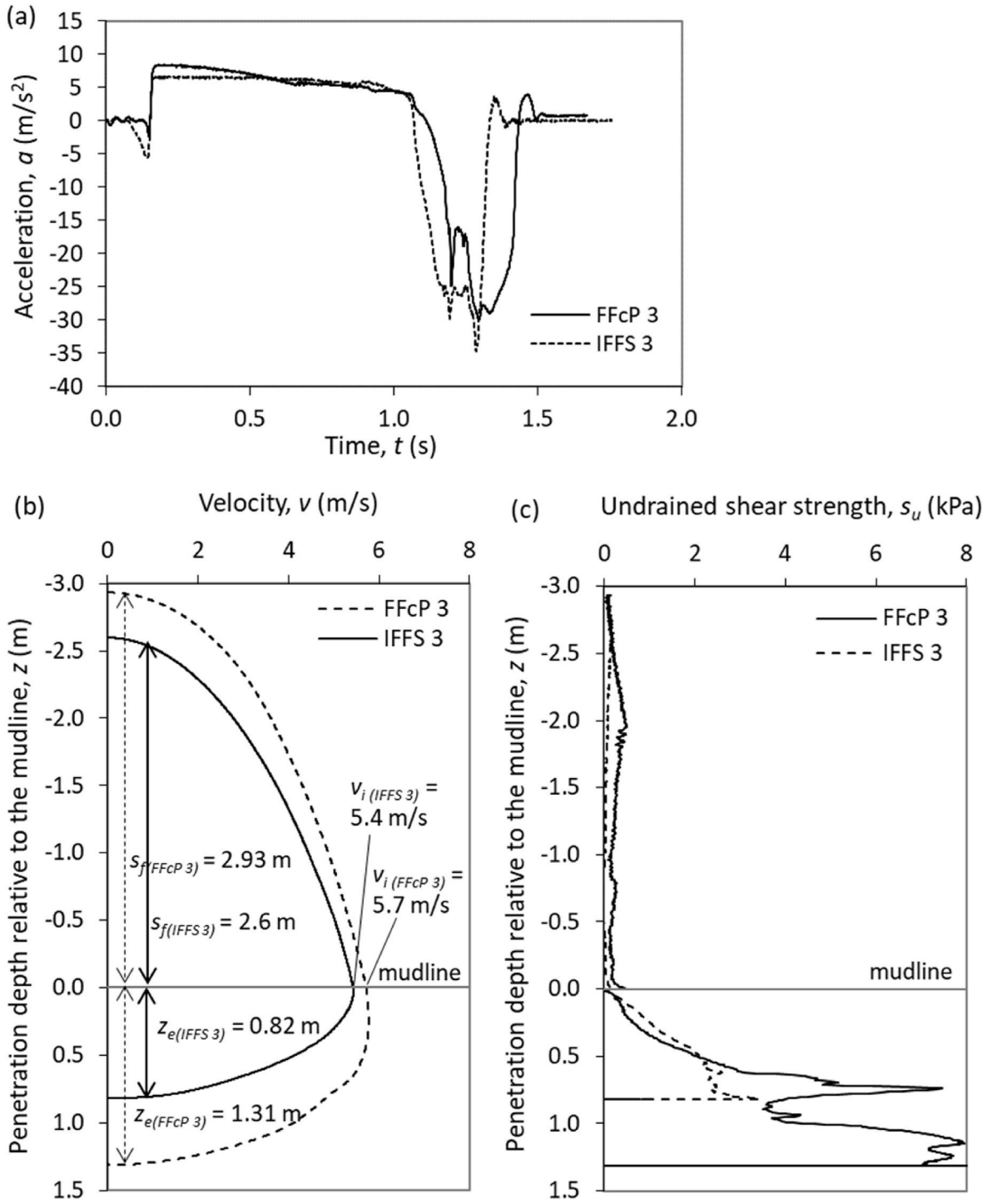

Fig. 10. Comparison between FFcP and IFFS: (a) acceleration signatures; (b) velocity profiles; (c) interpreted undrained shear strength profiles.

provided the contribution of rope drag is negligible. Fig. 9 compares measurements from tests IFFS 4 and IFFS 8 which involved similar drop heights and achieved similar impact velocities ($v_i = 4.7$ and 5 m/s), but at locations where the riverbed strength profile is markedly different. Fig. 9a shows a distinctly different acceleration signature in the two tests, with a peak deceleration, $a = 36$ m/s^2 in test IFFS 4 compared to a much higher and more rapid deceleration in test IFFS 8, with a peak value, $a = 151$ m/s^2. The deceleration signature and the peak deceleration have been proposed as a basis for sediment classification (e.g. Stoll, 2006; Stegmann et al., 2006). The smaller spread in the deceleration signature and the higher peak deceleration in test IFFS 8 indicates a much stronger sediment at this location than at IFFS 4, as also reflected in the interpreted s_u profiles in Fig. 9c. The stronger sediment resulted in a lower embedment depth, $z_e = 0.31$ m for IFFS 8, half of that in test IFFS 4 ($z_e = 0.68$ m), despite both tests achieving broadly similar impact velocities (Fig. 9b). In contrast, the peak deceleration in tests IFFS 4 and IFFS 5 are similar ($a = 36$ m/s^2, see Fig. 8), which results in similar peak $s_u \approx 3.5$ kPa in both tests.

The two penetrometers have approximately equal mass (IFFS: 29.4 kg; FFcP: 30.7 kg) but markedly different geometries. This is considered in Fig. 10 by comparing tests FFcP 3 and IFFS 3, which achieved similar impact velocities (FFcP 3: $v_i = 5.7$ m/s; IFFS 3: 5.4 m/s) and therefore

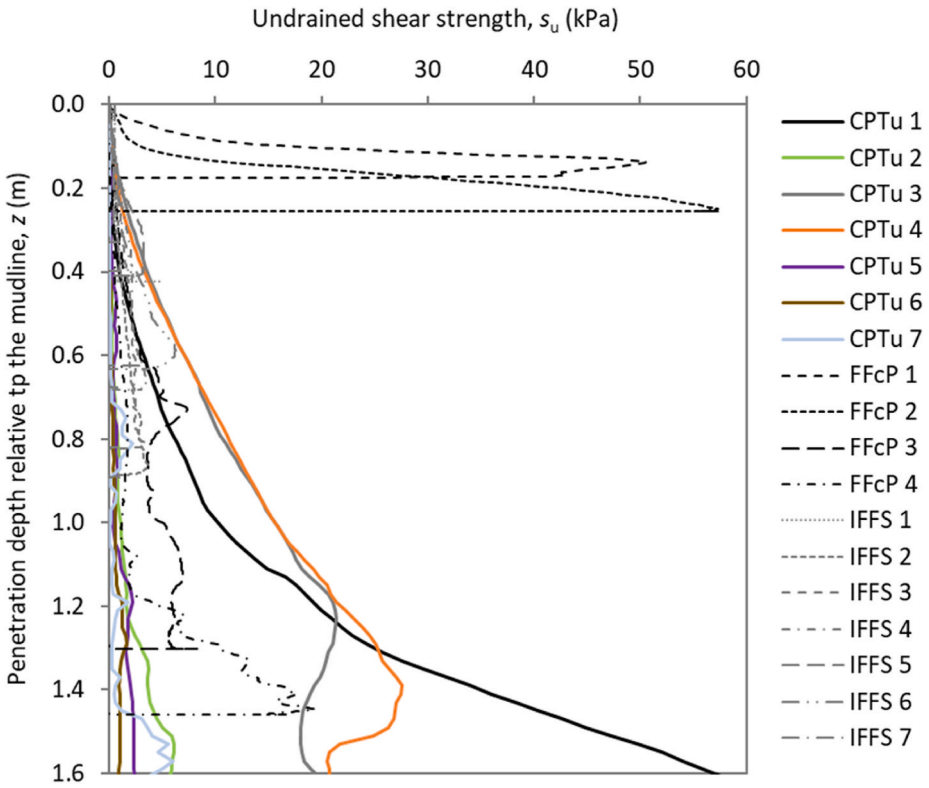

Fig. 11. Comparison between s_u profiles established from free-fall penetrometer tests and existing piezocone tests.

impact energy, and were tested at locations with similar sediment strength. The strength profiles from the two tests are broadly similar, but the FFcP achieved 60% higher embedment ($z_e = 1.31$ m), compared to the IFFS ($z_e = 0.82$ m). This aspect, linked to the smaller projected area of the FFcP, is considered later in the paper.

Fig. 11 shows s_u profiles derived from all FFcP and IFFS tests. Evidently the riverbed at the locations of FFcP 1 and FFcP 2 is much stronger than those at the other test sites, as $z_e < 0.25$ m, with peak s_u values of 51 and 57.8 kPa for FFcP 1 and FFcP 2, respectively. Embedment depths at the other locations were between 0.31 and 1.45 m, with back-figured s_u that increases by (on average) 3.5 kPa/m, such that the typical riverbed strength at these locations is $s_u < 20$ kPa.

Fig. 11 also compares FFP s_u profiles with those established from conventional piezocone tests. The piezocone tests (CPTu 1 to 7) were conducted onshore near the edge of the river as part of a previous site investigation (see Fig. 2 for locations), and utilised a 10 cm^2 cone, penetrated at the standard 20 mm/s. The equivalent normally consolidated $s_{u(CPTu,NC)}$ profiles in the riverbed (taking into consideration the apparent over-consolidation effects due to the onshore fill above the mudline) are estimated using the SHANSEP equation (Ladd and Foott, 1974):

$$s_{u(CPTu,NC)} = \sigma'_v \left(\frac{s_u}{\sigma'_v}\right)_{OC} \Big/ \mathrm{OCR}^n \tag{13}$$

where $(s_u/\sigma'_v)_{OC}$ is the over-consolidated strength ratio derived from the onshore piezocone test, σ'_v is the vertical effective stress in the riverbed, OCR is the overconsolidation ratio taken as the ratio of the pre-consolidation stress, σ'_p (taken as overburden pressure of the onshore fill) over the vertical effective stress, σ'_v, and n is the SHANSEP parameter taken as 0.94 for intact Burswood clay established from anisotropically consolidated triaxial compression tests (Low et al., 2011). For each piezocone test, the thickness of the onshore fill is determined as the distance of piezocone zero depth (shore surface) to water table/surface, plus the water depth of 3.35 m (averaged from all free-fall tests).

Fig. 11 shows that both FFPs yield comparable s_u profiles that are bound by the s_u determined from the net piezocone resistance. The s_u profiles derived from the piezocone and from the FFPs exhibit similar scatter, reflecting the lateral spatial variability in the sediment. As noted earlier in the paper, the main uncertainty when calculating s_u from a piezocone test is the choice of N_{kt} factor. This uncertainly also applies to interpretation of FFcP data, but with added uncertainties associated with the choice of strain rate parameters for bearing and frictional resistance, drag coefficient and interface friction ratio. There are fewer additional uncertainties in the interpretation of IFFS data, as the spherical geometry avoids the complication of considering frictional resistance and its variation with strain rate. Hence interpretation of IFFS data requires that N_c, β_{bear}, C_D and C_m are selected, whereas the equivalent interpretation of FFcP data requires N_{kt}, β_{bear}, β_{frict}, α and C_D to be selected. However, the magnitude of C_D (for both the IFFS and the FFcP) and C_m are mainly controlled by the penetrometer geometry, such that there is little uncertainty in their values. As selection of N_c and N_{kt} (for the IFFS and FFcP respectively) is also required for a static push-in penetrometer test, the additional uncertainty that the freefall penetrometer tests introduce is selection of β_{bear} for the IFFS test and β_{bear}, β_{frict} and α for the FFcP test. Equations (5) and (6) indicate that an appropriate value for $(v/d)_{\mathrm{ref}}$ also needs to be selected, but the approach considered here is to analyse the freefall data to produce an s_u profile that is comparable to the push-in test, such that $(v/d)_{\mathrm{ref}}$ would be based on the velocity and diameter of the push-in test, both of which are known.

To explore the sensitivity of the selection of β_{bear}, β_{frict} and α on the resulting s_u profiles, a (reported) range for each parameter was considered as shown in Fig. 12 and Table 3. Fig. 12 shows the influence of varying β_{bear}, β_{frict} and α on the derived s_u profile for Test FFcP 3. Adjusting β_{bear} from 0.035 to 0.085 results in a ±13% maximum variation in s_u (relative to the nominated parameters in Table 2), reducing slightly to ±10% for $\beta_{frict} = 0.18$ to 0.24. The slightly higher variation in s_u for β_{bear} reflects the slightly wider range considered for this parameter, although the ratio of the tip area to the side wall area also affects the

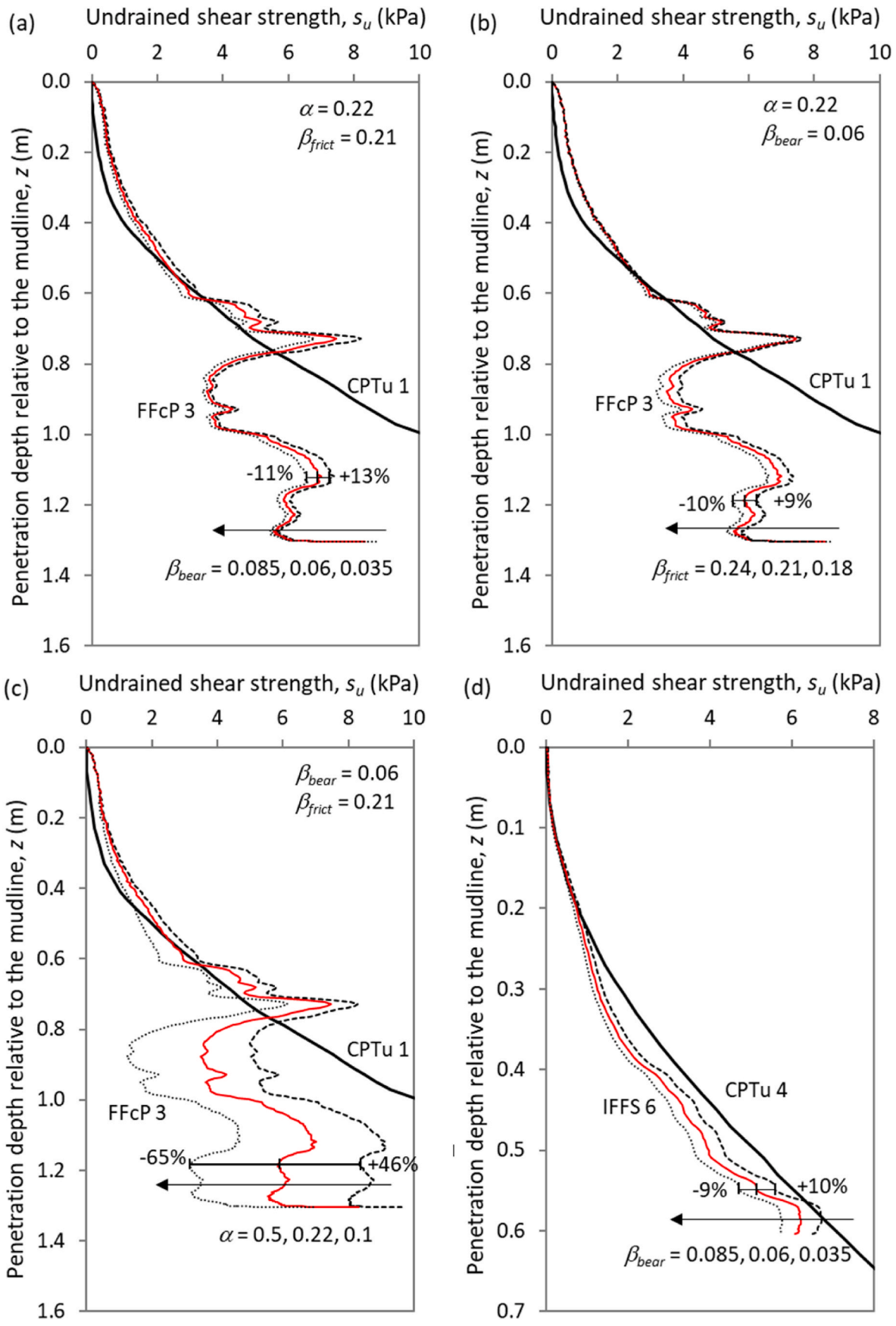

Fig. 12. Effect of varying model parameters on s_u: (a) β_{bear} (FFcP 3) (b) β_{frict} (FFcP 3); (c) α (FFcP 3); and (d) β_{bear} (IFFS 6).

Table 3
Sensitivity of model parameters on s_u estimation.

Test	Model parameter	Range considered	Variation in s_u estimation (%)[d]
FFcP 3	β_{bear}	0.035 to 0.085[a]	±13
	β_{frict}	0.18 to 0.24[b]	±11
	α	0.1 to 0.5[c]	±65
IFFS 2	β_{bear}	0.035 to 0.085[a]	±10

[a] Measured in centrifuge free-fall piezocone tests in kaolin (Chow et al., 2017) and typical of that reported by others (e.g. 0.05 to 0.09, Chung et al. 2006; Low et al., 2008).
[b] Reported from laboratory and field studies (e.g. Dayal et al. 1975; Steiner et al. 2014; O'Loughlin et al. 2016; O'Beirne et al., 2017a; Chow et al., 2017).
[c] Estimated as the inverse of soil sensitivity, $S_t = 2$ to 10.
[d] Relative to the nominated parameter values in Table 2.

sensitivity of s_u to each strain rate parameter. Adjusting α from 0.1 to 0.5 has a much more significant effect, causing up to ±65% variation in s_u. There is an even higher variation of up to ±76% when the limits on β_{frict} and α are paired (i.e. $\beta_{frict} = 0.18$ combined with $\alpha = 0.1$ and $\beta_{frict} = 0.24$ combined with $\alpha = 0.5$), similar to the 75% error noted by Chow et al. (2017) when the parameters controlling the magnitude of the dynamic frictional resistance needed to be selected 'blind'. This aspect of the interpretation can be removed if the FFcP is instrumented with a load cell to measure directly the tip resistance and a pore pressure sensor to measure pore pressure at the u_2 position, which would reduce the error from 75% to 10% (Chow et al., 2017). The dynamic frictional resistance could also be minimised for the FFcP by adopting a tapered body (e.g. Stark et al., 2017). This allows for an interpretation that avoids consideration of frictional resistance, which was shown by Chow et al. (2017) to reduce the inaccuracy in s_u determined from FFcP measurements to ±10%. Fig. 12d examines the sensitivity of the choice of strain rate parameter on s_u as derived from Test IFFS 6. Adjusting β_{bear} from 0.035 to 0.085 (i.e. as done for the FFcP) causes up to ±10% variation in s_u, slightly lower than that for the FFcP.

Table 3 summarises the sensitivity of the derived s_u value to these inputs. Evidently, the effect of parameter uncertainty is lowest for the IFFS. This beneficial aspect of the IFFS is offset somewhat by the lower penetration potential of the IFFS relative to the FFcP (see Fig. 10). Hence, there is a tradeoff to be considered with respect to the relative merit of the two penetrometers.

6. Embedment potential of free-fall penetrometers

A further comparison between the two penetrometer types is of their maximum achievable embedment. This must encompass the depth of interest, which may be a few centimetres for a habitat survey, or up to a metre or more for pipeline or cable routes. The maximum embedment can be estimated via a forward analysis of the equations of motion in Eqs. (2) and (9), following the approach adopted for predicting the embedment depth of projectiles or dynamically installed anchors (e.g. True, 1976; O'Loughlin et al., 2013; O'Beirne et al., 2017b). The mass, m of the penetrometers is controlled by the diameter, d, with the constraint that $L/d = 10$ for the FFcP (as per the geometry of the device considered in the field tests) and assuming that the penetrometers were solid stainless steel (ignoring the instrumentation void which reduces the net density of the penetrometer).

Ranges in penetrometer diameter, $d = 0.05$–0.2 m for the FFcP and $d = 0.1$–0.4 m for the IFFS were considered, such that the corresponding masses varied in the range $m = 7$–465 kg for the FFcP and $m = 4$–263 kg for the IFFS. The factor 4 range in diameter gives a factor 64 range in mass. Undrained shear strength, s_u, was assumed to vary linearly with depth according to kz with zero strength at the mudline and k taken in the range 1–10 kPa/m, for the purposes of exploring the effect of penetrometer geometry. Impact velocities in the range $v_i = 1$–13 m/s

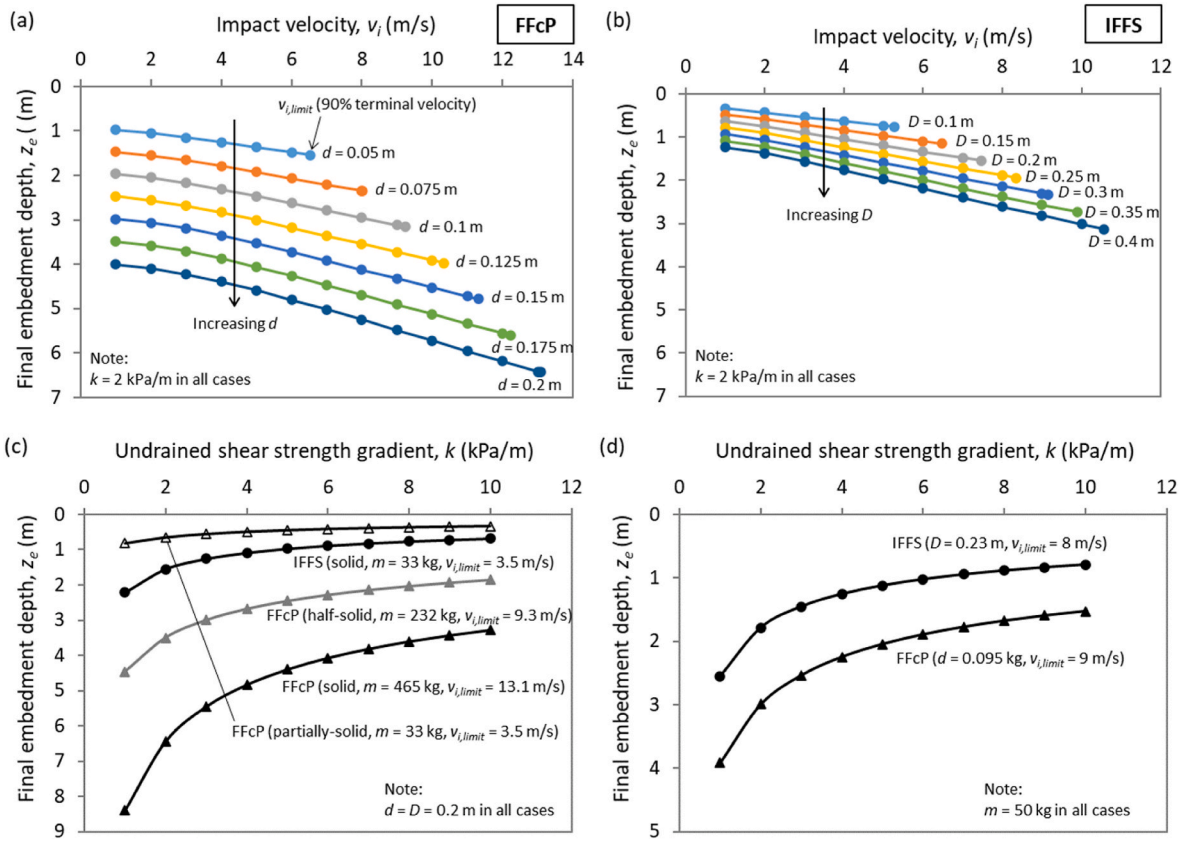

Fig. 13. (a, b) Influence of impact velocity; and (c, d) Influence of undrained shear strength gradient on final embedment of free-fall penetrometers examined through forward analysis of Eq. (2) and Eq. (9).

were considered, with the upper end of the range limited to 90% of the terminal velocity for that particular penetrometer mass.

Fig. 13 shows the effect of adjusting the independent variables (*d or D, k, v_i*) on final embedment, z_e, using the model parameters established previously for the FFcP ($N_{kt} = 11.2$, $\alpha = 0.22$, $\beta_{bear} = 0.06$, $\beta_{frict} = 0.21$, and $C_D = 1.2$) and for the IFFS ($N_c = 10.9$, $\beta_{bear} = 0.06$ and $C_D = 0.26$). The results on Fig. 13 support the field observations, in that embedment is shallower for the IFFS than for the FFcP, reflecting primarily the higher projected area and therefore proportionally higher penetration resistance.

The influence of impact velocity, v_i, on z_e for the FFcP and IFFS penetrating a sediment with an undrained shear strength gradient, $k = 2$ kPa/m is illustrated in Fig. 13a and b respectively. z_e increases non-linearly with increasing v_i and penetrometer diameter, d or D and hence mass, m. The rate of increase in z_e with v_i is higher for the IFFS than the FFcP and increases marginally with increasing diameter, reflecting the higher strain rate effect on shaft resistance that impedes the FFcP. Over the range of impact velocities considered ($v_i = 1$ m/s to 90% of the terminal velocity), z_e for the FFcP increases by a factor of 1.58–1.61, but by a factor of 2.29–2.53 for the IFFS.

For the FFcP and $k = 2$ kPa/m, an increase in diameter from $d =$ 50–200 mm, increases the limiting impact velocity from $v_{i,limit} =$ 6.5–13.1 m/s and the associated embedment depth from $z_e = 1.55$–6.44 m (i.e. by a factor of 4.2). The equivalent comparison for the IFFS (i.e. increasing D from 100 to 400 mm) causes $v_{i,limit}$ to increase from 5.3 to 10.6 m/s and z_e from 0.76 to 3.13 m (i.e. by a factor of 4.1). A similar analysis at a constant impact velocity, $v_i = 4$ m/s, shows an increase in z_e by a factor of 3.5 and 2.4 for the FFcP and IFFS respectively.

These factors of ~4 gain in z_e from a factor 4 increase in diameter can be approximated from energy considerations, neglecting the strain rate and soil drag terms. The overall energy balance of impact energy vs. energy dissipated through soil end bearing resistance can be expressed as:

$$\frac{1}{2}mv_{i,limit}^2 = \frac{1}{2}A_b N \overline{s_u} z_e \tag{14}$$

Since $m \propto d^3$ and $v_{i,limit}^2 \propto d$, the impact energy scales with d^4. Also, $A_b \propto d^2$ and since the soil strength increases linearly with depth, the average value, $\overline{s_u} \propto z_e$. Consequently, if rate effects are ignored, and if the soil resistance is dominated by the base, the maximum depth is proportional to the penetrometer size. The detailed analyses in Fig. 13a and b shows the additional influence of rate effects, beyond the general trend of this approximate analysis.

The influence of undrained shear strength gradient, k, is examined in Fig. 13c by considering z_e at $v_{i,limit}$ for $d = D = 0.2$ m with various m (i.e. varying the penetrometer solid content). From the energy balance above, $z_e \propto 1/\sqrt{k}$, but Fig. 13 captures the additional influences of rate effects and shaft friction, which alter the trend slightly. The results in Fig. 13c consider a solid IFFS and a partially solid FFcP with identical m = 33 kg, a half-solid FFcP ($m = 232$ kg) and fully solid FFcP ($m = 465$ kg) to explore further the role of mass in z_e, and also in recognition that an FFcP may need to be bottom heavy to maintain verticality during free-fall.

Embedment depth is seen to decrease non-linearly with increasing strength gradient at a rate that is slightly higher for the heavier (FFcP) penetrometer. z_e for a fully-solid FFcP is higher than that for the IFFS by a factor of between 3.8 and 4.8 (increasing with k), reducing to between 2.0 and 2.7 for the half-solid FFcP. Comparing both penetrometers with the same mass shows that the IFFS embeds further (by a factor of between 2.1 and 2.7, increasing with reducing k), which is due to the increased frictional resistance that develops along the FFcP shaft. However, Fig. 13d shows that when both penetrometers are fully solid, but with a diameter, $d = 0.09$ m for the FFcP and $d = 0.2$ m for the IFFS, such that they have the same mass, $m = 50$ kg, the FFcP embeds further than the IFFS, by a factor of between 1.5 and 1.9 (increasing with k). Although the total energy of both penetrometers at the mudline is approximately the same (as both have the same mass and the limiting impact velocity differs by only 1 m/s), the work needed to dissipate this energy is reached at a deeper embedment for the FFcP due to the reduced contact area (in bearing and friction).

In summary, the observations made from this simple parametric study are consistent with the field measurements, but also provide a basis for selecting an appropriately dimensioned free-fall penetrometer for expected field conditions. Final embedment depth is governed more by mass than impact velocity, consistent with findings reported in O'Loughlin et al. (2013), such that there is a greater benefit in maximising mass than in raising the drop height (e.g. by limiting voids within the penetrometer).

7. Conclusions

This paper has demonstrated the relative merit of cone and spherical free-fall penetrometers as site investigation tools for water environments. The sediment strength of a riverbed was determined from the penetrometer acceleration measurements using a framework that accounts for hydrodynamic drag and added mass (in the case of the spherical penetrometer) and the strain-rate enhanced geotechnical resistance. Comparisons between these strength estimates and those determined from push-in cone penetrometer tests are generally favourable, and also demonstrate the variability in the sediment strength of the riverbed. This can be quantified more readily and cost-effectively by free-fall penetrometer tests than push-in penetrometer tests.

Uncertainty in the model parameters leads to less variation in the deduced sediment strength for the IFFS than the FFcP, due to difficulties in quantifying the FFcP dynamic frictional resistance reliably. Whilst the IFFS has the benefit of a simpler interpretation that avoids the complication of quantifying dynamic shaft resistance, its embedment potential is lower. This tradeoff between accuracy and embedment potential needs to be considered in the context of sediment depth of interest. The models described here to back-analyse sediment strength can be used in a forward analysis to estimate embedment potential for a range of expected sediment strengths and penetrometer geometries, which provides a basis for selecting (or designing) an optimal free fall penetrometer for a given application.

CRediT authorship contribution statement

S.H. Chow: Conceptualization, Methodology, Investigation, Formal analysis, Writing – original draft, Supervision. **C.D. O'Loughlin:** Writing – review & editing, Methodology, Supervision, Resources. **C.L.V. Goh:** Methodology, Investigation. **R. McIlduff:** Methodology, Investigation. **D.J. White:** Writing – review & editing, Supervision, Resources, Funding acquisition. **F.C. Chow:** Resources, Writing – review & editing.

Declaration of competing interest

The authors declare that they have no known competing financial interests or personal relationships that could have appeared to influence the work reported in this paper.

Data availability

Data will be made available on request.

Acknowledgements

The field work was supported by the Woodside RiverLab initiative with The University of Western Australia, which aims to develop innovations in offshore engineering via research, education and outreach.

Development and fabrication of the free-fall penetrometers was funded by the Remote Intelligent Geotechnical Seabed Surveys (RIGSS) Joint Industry Project, supported by Fugro, Shell, Total and Woodside Energy Ltd. The second author acknowledges the support provided by the ARC ITRH for Transforming energy Infrastructure through Digital Engineering (TIDE, http://TIDE.edu.au) which is led by The University of Western Australia, delivered with The University of Wollongong and several other Australian and International research partners, and funded by the Australian Research Council, INPEX Operations Australia, Shell Australia, Woodside Energy, Fugro Australia Marine, Wood Group Kenny Australia, RPS Group, Bureau Veritas and Lloyd's Register Global Technology (Grant No. IH200100009).

References

Albatal, A., Stark, N., Castellanos, B., 2020. Estimating in situ relative density and friction angle of nearshore sand from portable FFP tests. Can. Geotech. J. 57, 17–31.

Blake, A.P., O'Loughlin, C.D., 2015. Installation of dynamically embedded plate anchors as assessed through field tests. Can. Geotech. J. 52 (9), 1270–1282.

Blake, A., O'Loughlin, C.D., Morton, J., O'Beirne, C., Gaudin, C., White, D.J., 2016. In-situ measurement of the dynamic penetratino of free-fall projectiles in soft soils using a low cost inertial measurement unit. Geotech. Test J. 39 (2), 235–251.

Chow, S., Airey, D., 2014. Free-falling penetrometers: a laboratory investigation in clay. J. Geotechn. Geoenviron. Eng. ASCE 140 (1), 201–214.

Chow, S.H., Loughlin, C.D.O., White, D.J., Randolph, M.F., 2017. An extended interpretation of the free-fall piezocone test in clay. Geotechnique 67 (12), 1090–1103.

Chow, S.H., O'Loughlin, C.D., Randolph, M.F., 2014. Soil strength estimation and pore pressure dissipation for free-fall piezocone in soft clay. Geotechnique 64 (10), 817–827.

Chung, S.F., Randolph, M.F., Schneider, J.A., 2006. Effect of penetration rate on penetrometer resistance in clay. J. Geotech. Geoenviron. Eng., ASCE 132 (9), 1188–1196.

Dayal, U., Allen, J.H., 1973. Instrumented impact cone penetrometer. Can. Geotech. J. 10, 397–409.

Dayal, U., Allen, J., Jones, J., 1975. Use of an impact penetrometer for the evaluation of the in-situ strength of marine sediments. Mar. Georesour. Geotechnol. 1 (No. 2), 73–89.

Guo, X., Nian, T., Wang, D., Gu, Z., 2022. Evaluation of undrained shear strength of surficial marine clays using ball penetration-based CFD modelling. Acta Geotechnica 17, 1627–1643.

Jeanjean, P., Spikula, D., Young, A., 2012. Technical vetting of free-fall cone penetrometer. In: Proceedings Of7th International Offshore Site Investigation and Geotechnics Conference: Integrated Geotechnologies – Present and Future. Society for Underwater Technology, London, U.K., pp. 15–18

Ladd, C.C., Foott, R., 1974. New design procedure for stability of soft clays. J. Geotech. Eng. Div. 100 (7), 763–786.

Low, H.E., Randolph, M.F., DeJong, J.T., Yafrate, N.J., 2008. Variable rate full-flow penetration tests in intact and remoulded soil. In: Proceedings of the 3rd International Conference on Geotechnical and Geophysiscal Site Characterization, pp. 1087–1092. Taipei.

Low, H.E., Landon Maynard, M., Randolph, M.F., DeGroot, D.J., 2011. Geotechnical characterisation and engineering properties of Burswood clay. Geotechnique 61 (7), 575–591.

Morton, J.P., O'Loughlin, C.D., White, D.J., 2016a. Estimation of soil strength in fine-grained soils by instrumented free-fall sphere tests. Geotechnique 66 (12), 959–968.

Morton, J.P., O'Loughlin, C., White, D., 2016b. Centrifuge modelling of an instrumented free-fall sphere for measurement of undrained strength in fine-grained soils. Can. Geotech. J. 53 (ja), 918–929.

O'Beirne, C., O'Loughlin, C.D., Gaudin, C., 2017a. Assessing the penetration resistance acting on a dynamically installed anchor in normally consolidated and overconsolidated clay. Can. Geotech. J. 54, 1–17.

O'Beirne, C., Loughlin, C.D.O., Gaudin, C., 2017b. A release-to-rest model for dynamically installed anchors. J. Geotechn. Geoenviron. Eng. ASCE 143 (9), 04017052.

O'Loughlin, C.D., Blake, A.P., Gaudin, C., 2016. Towards a simple design procedure for dynamically embedded plate anchors. Géotechnique 66 (9), 741–753.

O'Loughlin, C.D., Richardson, M.D., Randolph, M.F., Caudin, C., 2013. Penetration of dynamically installed anchors in clay. Géotechnique 63 (No. 11), 909–919.

Peuchen, J., Looijen, P., Stark, N., 2017. Offshore characterisation of extremely soft sediments by free fall penetrometer. In: Offshore Site Investigation and Geotechnics: Smarter Solutions for Future Offshore Developments: Proc. 8th Intl. Conf. Royal Geographical Society, ume 1. Society for Underwater Technology, London, pp. 370–377.

Randolph, M.F., Gaudin, C., Gourvenec, S.M., White, D.J., Boylan, N., Cassidy, M.J., 2011. Recent advances in offshore geotechnics for deep water oil and gas developments. Ocean Eng. 38 (7), 818–834.

Randolph, M.F., Stanier, S.A., O'Loughlin, C.D., Chow, S.H., Bienen, B., Doherty, J.P., Mohr, H., Ragni, R., Schneider, M.A., White, D.J., Schneider, J.A., 2018. Keynote Lecture: penetrometer equipment and testing techniques for offshore design of foundations, anchors and pipelines. In: *Proceedings Of the 4th International Symposium On Cone Penetration Testing (CPT'18)* (accepted for publication.

Richardson, M.D., 2008. Dynamically installed anchors for floating offshore structures. In: PhD thesis. The University of Western, Australia.

Stark, N., Kopf, A., Hanff, H., Stegmann, S., Wilkens, R., 2009. Geotechnical investigations of sandy seafloors using dynamic penetrometers. In: OCEANS 2009, MTS/IEEE Biloxi - Marine Technology for Our Future: Global and Local Challenges, pp. 1–10 (Biloxi, MS).

Stark, N., Radosavljevic, B., Quinn, B., Lantuit, H., 2017. Application of portable free-fall penetrometer for geotechnical investigation of Arctic nearshore zone. Can. Geotech. J. 54, 31–46.

Stegmann, S., Morz, T., Kopf, A., 2006. Initial Results of a new Free Fall-Cone Penetrometer (FF-CPT) for geotechnical in situ characterisation of soft marine sediments. Nor. Geol. Tidsskr. 86 (3), 199–208.

Steiner, A., Kopf, A.J., L'Heureux, J.-S., Kreiter, S., Stegmann, S., Haflidason, H., Moerz, T., 2014. In situ dynamic piezocone penetrometer tests in natural clayey soils–a reappraisal of strain-rate corrections. Canadian Geotech. J. 51, 272–288.

Stephan, S., Kaul, N., Villinger, H., 2012. The Lance Insertion Retardation meter (LIRmeter): an instrument for in situ determination of sea floor properties—technical description and performance evaluation. Mar. Geophys. Res. 33 (3), 209–221.

Stoll, R.D., 2006. Measuring sea bed properties using static and dynamic penetrometers. In: Proc. ASCE International Conference Civil Engineering Oceans VI, pp. 386–395.

Sumer, B.M., Fredsoe, J., 1997. Hydrodynamics Around Cylindrical Structures. World Scientific, Singapore.

True, D.G., 1976. Undrained vertical penetration into ocean bottom soils. In: PhD thesis. University of California, Berkeley.

Young, A.G., Bernard, B.B., Remmes, B.D., Babb, L.V., Brooks, J.M., 2011. CPT stinger " - an innovative method to obtain CPT data for integrated geoscience studies. In: Offshore Technology Conference, pp. 1–10 (Houston, Texas, United States).